Evolution of the Interface and Metal Film Morphology in the Vapor Deposition of Ti on Hexadecanethiolate Hydrocarbon Monolayers on Au

Timothy B. Tighe, Thomas A. Daniel, Zihua Zhu, Sundarajan Uppili, Nicholas Winograd,* and David L. Allara*

Department of Chemistry and The Materials Research Institute, Pennsylvania State University, University Park, Pennsylvania 16802

Received: July 28, 2005; In Final Form: September 4, 2005

The combination of in situ X-ray photoelectron spectroscopy, infrared reflection spectroscopy, atomic force microscopy, and time-of-flight secondary ion mass spectrometry are used to probe the nature of the evolving interface chemistry and metal morphology arising from Ti vapor deposition onto the surface of a $CH_3(CH_2)_{15}S$/Au{111} self-assembled monolayer (SAM) at ambient temperature. The results show that for a deposition rate of ~0.15 Ti atom·nm^{-2}·s^{-1} a highly nonuniform Ti overlayer is produced via a process in which a large fraction of impinging Ti atoms do not stick to the bare SAM surface. The adsorbed atoms form isolated Ti clusters and react with CH_3 groups to form carbide products at the cluster−SAM interfaces. Further growth of Ti clusters appears to be concentrated at these scattered reaction centers. The SAM molecules in the local vicinity are subsequently degraded to inorganic products, progressing deeper into the monolayer as the deposition proceeds to give an inorganic/organic nanocomposite. A continuous overlayer does not form until metal coverage approaches ~50 Ti atoms per SAM molecule. These data indicate that for applications such as molecular device contacts the use of Ti may be highly problematic, suffering from both a highly nonuniform contact area and the presence of extensive inorganic products such as nonstoichiometric carbides and hydrides.

1. Introduction

The vacuum deposition of metal layers on organic thin films is a widely used process for many applications ranging from electronic devices to barrier coatings. Predictions of the outcome of any particular deposition are typically very difficult because of the lack of fundamental information on the complex, intertwined chemical and physical processes that can be involved in interface formation and metal overlayer growth. As a means of building fundamental rules underlying these complex phenomena, recent efforts have focused on using the chemically and physically well-defined structures of self-assembled monolayers (SAMs) as the organic substrates.[1−8] These structures not only provide model systems but also have become highly relevant because of their recent applications in molecular electronic devices, where vapor-deposited metal contacts are used in a base electrode−molecule−metal structure[9−29] for which the exact nature of the contact interface and metal morphology can profoundly affect device performance.

When metal atom vapors impinge on organic substrates, a wide range of behaviors are possible, many often undesired, including severe chemical degradation, clustering of the metal into nonuniform, heterogeneous overlayers with discontinuous interfaces, penetration deep into the organic matrix, and even scattering from the surface with no condensation. For a number of applications it is desirable to achieve reproducibly uniform deposition across the surface with subsequent growth of a dense, uniform metal overlayer. One potential path for achieving this structure might seem to be the deposition of metal atoms that exhibit chemical reactivity with the ambient surface of the organic substrate, based on the simple notion that uniform reaction across the surface should lead to a uniform nucleation and growth. Recent reports, however, demonstrate cases where this picture does not completely hold. For example, in the case of Al vapor deposition on a methyl ester-terminated hexadecanethiolate/Au{111} SAM, it was observed that while the initially deposited Al atoms react quantitatively with the ester groups in a 1:1 stoichiometry, subsequent deposition produces several layers of a dielectric form of the Al, followed by an ~3 nm highly porous metallic phase and a final dense metal overlayer.[3] In contrast, for Al deposited on H_3C- or H_3CO-terminated hexadecanethiolate/Au{111} SAMs, there are no chemical reactions and the Al atoms partition to different extents between penetration to the Au/S interface to form an adlayer and growth of an overlayer at the SAM surface.[3,5] These data show that Al, typically considered a chemically reactive metal in terms of its thermochemical ability to form highly stable oxides and carbides, appears, in fact, to be dominantly controlled by subtle kinetic factors in its interactions with SAM surfaces. In view of this, it is of significant interest to explore the behavior of other common, aggressively reactive metals to look for complexities in their deposition on organic materials. The specific example of Ti would appear to be a good starting point because of the well-known aggressive chemical character of Ti and its common use in microelectronics processing,[30,31] extended more recently as a top contact in molecule-based electronics.[9,11,12,16,17,20,21,23−28]

Pointing to the aggressive nature of Ti, the vapor-deposited metal reacts indiscriminately with triazine, polyimide, polystyrene, polyethylene, and epoxy films to form Ti−O, Ti−C, and Ti−N bonds[30−34] and with fluoropolymers to form Ti−C, Ti−O, and Ti−F bonds.[35] In previous work[36] we showed from XPS data for ambient-temperature substrates that Ti reacts with the terminal groups of $-CO_2H$, $-CO_2CH_3$, $-CH_3$, $-OH$, and

* Corresponding authors: e-mail dla3@psu.edu (D.A.) or nxw@psu.edu (N.W.).

10.1021/jp054174k CCC: $30.25
Published on Web 00/00/0000 PAGE EST: 8.6

−CN-terminated alkanethiolate SAMs and concluded further that Ti readily reacts with the $-CH_2-$ moieties of alkyl chains, which should be the least reactive groups of typical organic molecules. In a recent report, de Boer et al.,[24] as a control to their larger study on vapor-deposited Au, Al, and Ti on SAMs of conjugated mono- and dithiols, also examined the interaction of Ti with the -CH_3-terminated hexadecanethiolate/Au{111} SAM. Using infrared reflection spectroscopy (IRS) evidence, they found Ti to be highly reactive and destructive. Despite this pattern of aggressive reactivity from both XPS and IRS studies, however, the preliminary data from our earlier XPS study[36] also suggest that in the initial stages of deposition on the $-CH_3$-terminated hexadecanethiolate/Au{111} SAM a fraction of the incoming Ti atoms striking the surface scatter back into the vacuum with no reaction, while the adsorbed remainder do not nucleate uniformly across the surface but rather form isolated clusters. While such scattering has been noted for unreactive atoms such as noble metals,[37] this behavior is not expected for aggressively reactive atoms.

Overall, these limited data suggest the $-CH_3$-terminated SAM shows a range of behaviors in Ti vapor deposition that are controlled by kinetic processes as well as thermochemical driving forces. Given the recent interest in using Ti metal as a top contact for device structures with hydrocarbon-like top layers[11,20,21,24−28] and our own work in optimizing the top contacts in molecular electronic devices (e.g., see ref 7), there was significant motivation to explore in greater detail the processes involved in Ti deposition on alkyl chain monolayers and relate this to the desirable characteristics for high-quality contacts. The results of our study show that for deposition on a sample at room temperature with controlled Ti fluxes, Ti does indeed scatter off the CH_3 SAM surface, with a smooth decrease in the scattered fraction with increasing Ti doses, followed by gradual formation of a nonuniform interface. The overall structure consists of clusters of Ti atoms with metallic Ti outer regions and deep carbide interphases, which eventually, at total average coverages exceeding 50 Ti atoms per SAM molecule, merge into a continuous overlayer. These results underscore the need to understand how the interplay between kinetic and thermochemical pathways can affect the physical and chemical characteristics of deposited top metal layers on organic films for applications such as molecular devices.

2. Experimental Section

2.1. Materials and General Procedures. Details of the synthesis of $D_3C(CD_2)_7(CH_2)_8S$/Au SAM can be found in the Supporting Information. The preparation and characterization of the $H_3C(CH_2)_{15}S$/Au and $D_3C(CD_2)_7(CH_2)_8S$/Au SAMs have been described in detail previously[38−42] and are summarized briefly here. Sequential thermal depositions of Cr (∼10 nm) and Au (∼200 nm) were made onto clean Si(001) native oxide covered wafers. Self-assembly of well-organized monolayers was achieved by immersing the Au substrates into millimolar solutions of the relevant alkanethiol molecules in absolute ethanol for ∼2 days at ambient temperature. The monolayer films were characterized with single-wavelength ellipsometry, infrared spectroscopy, and contact angle measurements to ensure that they were densely packed, clean surfaces. In addition, all SAMs were characterized by the initial time-of-flight secondary ion mass spectrometry (ToF−SIMS), infrared reflection spectroscopy, (IRS), and X-ray photoelectron spectroscopy (XPS) measurements prior to metal deposition.

Several sources were used for Ti (R. D. Mathis, Alfa Aesar) but in all cases the purities were ≥99.99%. The depositions were conducted with resistively heated tungsten baskets or Ti-coated tungsten wires with fluxes controlled to ∼0.15 atom·nm^{-2}·s^{-1} at the sample for all analysis methods. The throw distances were all >35 cm, and the sample temperatures remained near ∼25 °C under the deposition conditions. In all cases the mass of metal atoms delivered to the SAM surfaces was measured by placing quartz crystal microbalance (QCM) crystals with gold electrodes in the path of the vapor flux. Geometric factor corrections (tooling factors) for the placement of the QCM crystal relative to the sample and absolute fluxes were calibrated by use of atomic force microscopy (AFM) measured film thicknesses at the sample and QCM crystal locations. Readout/controller units were obtained from Maxtek, Inc. (TM-400; maximum error ±8%; ToF−SIMS setup) and Sigma Instruments (SQM-160, maximum error ±7%; IRS and XPS setup).

2.2. X-ray Photoelectron Spectroscopy. The XPS analyses were performed on a Kratos Analytical Axis Ultra instrument equipped with a monochromatic Al Kα source operating at an X-ray power of 280 W. Spectra were collected at a 90° photoelectron takeoff angle with respect to the sample plane, with a pass energy of 20 eV and an energy step of 0.15 eV. The resulting full width at half-maximum (fwhm) of the Au $4f_{7/2}$ line was 0.71 eV. All spectra were referenced to Au $4f_{7/2}$ at 84.0 eV. Following analysis of the uncoated monolayer, the samples were transferred under continuous vacuum to the deposition chamber, which was isolated from the analysis chamber by a gate valve. During the depositions the pressure remained $<1 \times 10^{-8}$ Torr. After deposition, the metal/SAM specimen was transferred directly in vacuo back to the analysis chamber, where the pressure was maintained below 5×10^{-9} Torr.

2.3. Infrared Spectroscopy. Analyses were performed on a Fourier transform instrument (Mattson Research Series 1000) fitted with custom in-house optics configured externally to the instrument and designed for grazing incidence reflection of samples under vacuum.[3−5,8] A liquid nitrogen-cooled mercury−cadmium−telluride (MCT) detector was used with an effective low-frequency cutoff of ∼750 cm^{-1}. The infrared beam passed through the analysis chamber through a pair of differentially pumped KBr windows. After analysis of the bare monolayer, a shield was moved to unblock the path between the sample and the metal source. The pressure remained $<3 \times 10^{-7}$ Torr during the deposition. The final spectra were determined as $-\log(R/R_0)$, where R is the sample spectrum and R_0 is the spectrum of a bare gold wafer or a $C_{16}D_{33}S$/Au{111} SAM, with a given reference chosen on the basis to maximize information in the specific spectral region of interest for a given sample.

2.4. Time-of-Flight Secondary Ion Mass Spectrometry. The ToF−SIMS analyses were performed on a custom-designed instrument as described previously.[43] Briefly, the instrument consists of a loadlock, a preparation chamber, a metal deposition chamber, and the primary analysis chamber, each separated by a gate valve. The primary Ga^+ ions were accelerated to 15 keV and contained in a 100 nm diameter probe beam, which was rastered over a (106 × 106) μm^2 area during data acquisition. All spectra were acquired at the static limit with a total ion dose of less than 10^{11} ions·cm^{-2}. Relative peak intensities are reproducible to within ± 8% from sample to sample and ± 8% from scan to scan. During deposition the pressure remained $<5 \times 10^{-8}$ Torr. After deposition, the preparation chamber pressure was allowed to recover to the base value of 1.5×10^{-9} Torr before sample transfer to the analysis chamber.

2.5. Atomic Force Microscopy. The AFM measurements were performed in an ultrahigh-vacuum (UHV) chamber (base

pressure 10^{-10} Torr) outfitted with a RHK 350 scan head setup which was controlled by a RHK SPM 100 electronics system (RHK Technologies, Troy, MI). The images were taken at 1 Hz line scan rates with silicon cantilevers in contact mode (FFM type, spring constant ~2.8 N/m, tip radius ~10 nm; Molecular Imaging, Tempe, AZ) with simultaneous lateral force mode images also recorded. Because of the constant vacuum conditions of the experiment during sequential dosing, the contact mode was optimal for surface imaging in our setup.[44] In addition, the mechanical response characteristics to surface features provided valuable information. The SAM was formed on Au(111) substrates on mica (Molecular Imaging, Tempe, AZ), which were hydrogen flame-annealed immediately prior to monolayer formation. Following in vacuo AFM analysis of the freshly made SAM, the samples were transferred under continuous vacuum to the deposition chamber, which was isolated from the analysis chamber by a gate valve. During the deposition, the pressure remained $<5 \times 10^{-8}$ Torr. The mass of the deposited Ti was obtained by use of a SAM-coated QCM electrode adjacent to the sample. After deposition, the metal/SAM specimen was transferred directly in vacuo back to the analysis chamber for immediate imaging, where the pressure was maintained below 5×10^{-10} Torr.

2.6. Definition and Measurement of Deposited Metal Coverage. The mass of metal condensed (equivalently, adsorbed or permanently deposited atoms) per unit area (ρ_A) on the samples was determined directly from the QCM measurements. For ease in data analysis and interpretation, an equivalent coverage of condensed metal atoms per SAM molecule (θ_{Ti}) was calculated from the ρ_A values and the molecular density of 4.6 molecules·nm^{-2} for a well-formed alkanethiolate/Au{111} SAM. It follows that our deposition flux of ~0.15 atom·nm^{-2}·s^{-1} is equivalent to ~0.033 Ti atom (SAM molecule)$^{-1}$ s^{-1}.

In the early stages of Ti deposition on the SAM, it was observed by XPS that only a fraction of the metal atom flux directed at the surface condensed, viz, some fraction of the incoming atoms was reflected from the surface back into the vacuum. To determine accurate condensation efficiencies, measurements were made of the sticking (or condensation) coefficients, defined as $S(\theta) \equiv \theta/\theta_0$, where θ is the actual number of condensed metal atoms per SAM molecule, as determined directly from the QCM ρ_A values, and θ_0 is the total number (dose) of incoming metal vapor atoms per SAM molecule, as dictated by the flux of atoms arriving at the surface. The experiments were conducted in a side-by-side, dual QCM setup with a SAM-covered Au QCM electrode and a reference bare Au electrode, predeposited with Ti.[45] The data (Figure 1) show an initial $S(\theta)$ value of ~0.1 with a subsequent smooth, asymptotic approach to $S(\theta) = 1.0$ at high doses. A cross check with coverages estimated from the XPS Ti 2p core level peak areas in the low-coverage region[46] is shown in Figure 1.

3. Results

3.1. X-ray Photoelectron Spectroscopy: Formation of Carbide Products. The constant binding energy for the Au $4f_{7/2}$ line (Figure 2, left) indicates negligible charging or alloying at the gold interface.[36] In the C 1s region (Figure 2, center) starting at $1.2 < \theta < 3.3$, a feature appears at 282.1 eV that is straightforwardly assigned to a carbide species.[30,36,47,48] Further deposition shows attenuation and broadening of the main -(CH_2)- C 1s feature and continued carbide growth.[36] The Ti 2p region (Figure 2, right) shows Ti appearing at low coverages (θ = 1.1). This is most easily seen for the stronger $2p_{3/2}$ feature of the Ti 2p doublet where a peak appears at 454.7 eV. This initial

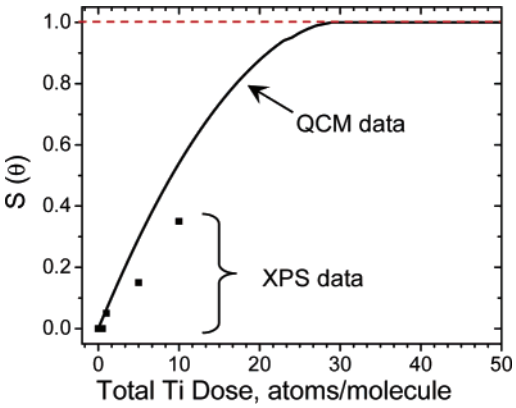

Figure 1. Sticking (condensation) coefficient $S(\theta)$ of Ti on the SAM surface vs total Ti dose delivered (atoms per SAM molecule) to the SAM surface for doses up to 50 atoms per molecule: (—) determined from a dual QCM experiment; (■) estimated from XPS Ti 2p peak areas. The red dotted line marks $S(\theta) = 1.0$. For details see text.

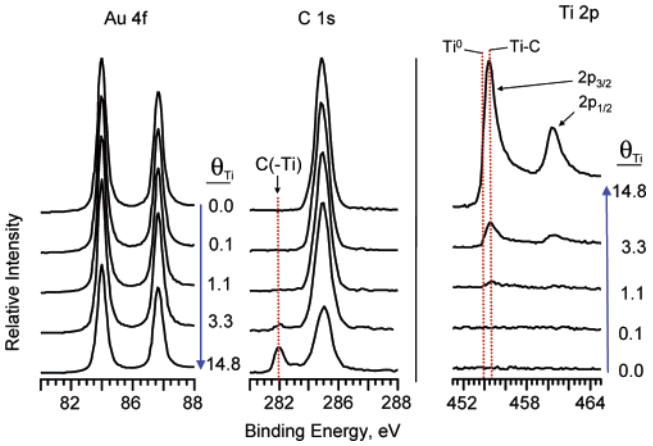

Figure 2. XPS Au 4f (left), C 1s (center), and Ti 2p (right) core level spectra as a function of incrementally increasing Ti coverage on the SAM surface, as determined from the total amount of metal delivered to the surface, corrected for the independently measured sticking coefficient. The intensity scales are in arbitrary units and are different for each core level. The dashed lines in the Ti $2p_{3/2}$ peak at 454.7 and 456.4 eV mark the positions for the metallic and carbide species. For details see text.

feature is assigned to Ti−C.[30,36,47,48] The positions and extent of carbide formation in the C 1s and Ti 2p regions agree well with our previously published results.[36] Looking at the Ti $2p_{3/2}$ feature in detail, as the deposition increases to θ = 14.8, the line shape becomes broader and asymmetric with intensity appearing on the low binding energy side (follow the line marked Ti^0 in the figure) and a markedly broad shoulder on the high-energy side of the main carbide peak. The low binding energy intensity we attribute to metallic Ti[30,36,47−49] and the high binding energy shoulder is assigned to a convolution of oxide species formed from background gases.[30,47−49] Further analysis of the Ti 2p spectra at these higher coverages was not done because of the interfering species formed by reaction of Ti with background gases.[50]

3.2. Infrared Reflection Spectroscopy: Ti Deposition on a $CD_3(CD_2)_7(CH_2)_8S$/Au SAM. "Top-Down" Localized Chemical Degradation. The experiments were carried out on SAMs prepared from $CD_3(CD_2)_7(CH_2)_8SH$ in order to allow the possibility of distinguishing between a laterally uniform, top-down or a cratering or pitting mechanism in the carbide formation (see XPS section). Detailed characterizations of the IR modes of C−H[38−42] and C−D[41,42] have been presented elsewhere. The relevant stretching modes for C−H (2800−3000

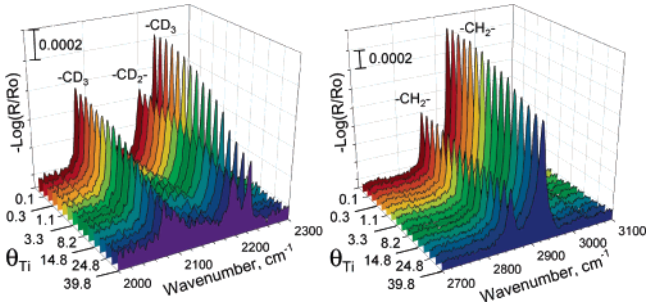

Figure 3. IRS C−H (right) and C−D (left) stretching mode spectra for a $CD_3(CD_2)_7(CH_2)_8S$/Au SAM at incrementally increasing Ti coverages (θ_{Ti}). The coverages were determined from the total amount of metal delivered to the surface corrected for the independently measured sticking coefficient. Only selected spectra are assigned θ_{Ti} labels for clarity. For details see text.

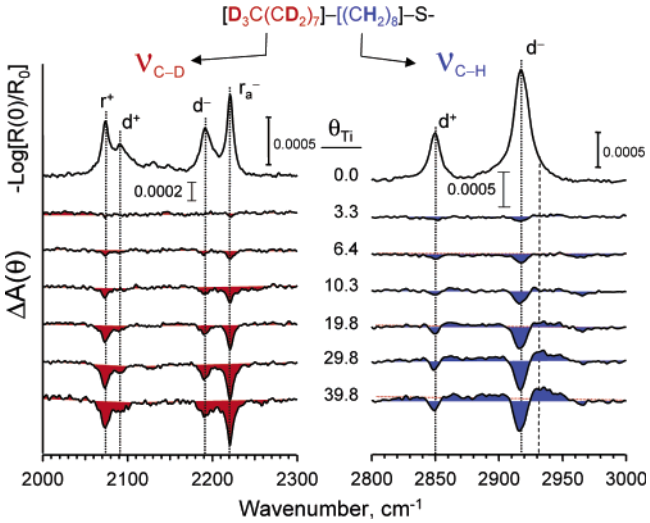

Figure 4. IRS C−H and C−D stretching mode spectra as a function of the incrementally increasing Ti coverage (θ_{Ti}) on a $CD_3(CD_2)_7(CH_2)_8S$/Au SAM surface as determined from the total amount of metal delivered to the surface corrected for the independently measured sticking coefficient. The $\theta_{Ti} = 0$ spectrum is shown in terms of the actual intensities, $-\log [R(0)/R_0]$, while for $\theta_{Ti} > 0$ difference spectra, defined as $\Delta A(\theta) = -\log [R(\theta_{Ti})/R(\theta_0)]$, are shown. Thus, increasing negative peaks signify a loss of the original peak intensity from the bare SAM. d and r represent methylene and methyl group stretching features, respectively. For details see text.

cm^{-1}) and C−D (2000−2300 cm^{-1}) are summarized for convenience: 2851 and 2918 cm^{-1},$-CH_2-$ symmetric C−H stretch (d^+) and $-CH_2-$ antisymmetric C−H stretch (d^-) modes, respectively; 2091 and 2192 cm^{-1}, $-CD_2-$ symmetric C−D stretch (d^+) and $-CD_2-$ antisymmetric C−D stretch (d^-) modes, respectively; and 2074 and 2221 cm^{-1}, $-CD_3$ symmetric C−D stretch (r^+) and $-CD_3$ antisymmetric C−D stretch (r_a^-) modes, respectively.

The overall data are shown in Figure 3, where the trends in peak intensities clearly show the $-CD_2-$ and $-CD_3$ modes rapidly losing intensity with increasing θ compared to the slow decay of the CH_2 modes. The attenuation of IR modes can be caused by chemical reactions, reorientation of the monolayer dipoles with respect to the surface,[51] or screening of the dipoles due to metal atoms, clusters, or overlayers.[51,22] Since the spectral intensities from the C−D and C−H segments decay at different rates, reorientation of the molecules can be eliminated and the low overlayer coverages of the metal are far too small for any significant electromagnetic field screening losses. Given the XPS evidence for carbide formation, it is clear that the major cause of the peak losses is chemical degradation, with possible minor contributions from more subtle effects such as line shape broadening. Since the $-C_8D_{17}$ segment, located at the outer SAM surface, is associated with the fastest intensity decay, one can readily conclude that significant chemical attack occurs at this segment. The particularly rapid decrease associated with the CD_3 group suggests this is the primary point of attack.[53]

To better reveal the changing character of the spectra, the data are plotted in Figure 4 in terms of absorbance difference spectra, $\Delta A(\theta)$, calculated as $-\log [R(\theta_{Ti})/R(\theta_0)]$, where θ_{Ti} represents the Ti-covered SAM and θ_0 represents the bare SAM, respectively. Note that negative $\Delta A(\theta)$ features indicate an intensity loss relative to the original SAM spectrum for a given Ti coverage.

In the C−D stretching region (Figure 4, left), representing the behavior of the top $-(CD_2)_7CD_3$ portion of the SAM, the small negative CD_3 mode peaks (2074 and 2221 cm^{-1}) barely appearing at $\theta_{Ti} = 3.3$ show that deposited Ti immediately interacts with the CD_3 group. At increasing Ti coverage, negative CD_2 peaks appear and continued deposition shows attenuation to both the original CD_2 and CD_3 mode intensities, with preferential attenuation to CD_3. By $\theta = 40.5$ the $CD_2(d^-)$ and $CD_3(r_a^-)$ intensities are attenuated to ∼35−40% and 50−60%, respectively. Since the exact stoichiometries of the reactions are uncertain, it is difficult to extract quantitative relative reactivities from these data. Given the 14/3 ratio of CD_2 to CD_3 bonds in $-(CD_2)_7CD_3$ and a faster attenuation of the CD_3 modes, though, it is clear that the Ti atoms favor reactions with the top CD_3 group,[53] which in turn supports a top-down degradation of the alkyl chain.

In the C−H stretching mode region (Figure 3, right), both mode intensities decrease at the same rate, as expected. The d^- mode intensity has decreased by ∼30% at $\theta = 40.5$. Note that this compares in magnitude roughly to the CD_2 d^- mode attenuation of ∼35−40%. Consistent with this parallel behavior, the attenuation for the d^- mode intensity at $\theta = 20.5$ is ∼0.2 for both the CD_2 and CH_2 modes. This comparison implies some chemical attack of Ti atoms is occurring at the bottom $-(CH_2)_8-$ chain units, as well as at the top of the SAM. Notice also, in contrast to the lack of positive $\Delta A(\theta)$ features in the C−D spectra, the C−H spectra show the growth of weak, but clearly observable, positive features at ∼2925−2935 cm^{-1}. These typically would correspond to the growth of conformational disorder in alkyl chains but also might be due to localized chemical degradation in portions of the molecules that produce contiguous carbide phases. Overall, the IR data point to a primary attack of Ti at the top of the chains with subsequent attack progressing into deeper regions of the SAM.

3.3 Atomic Force Microscopy: Ti Clustering and Overlayer Morphology. Prior to metal deposition, images were taken to confirm the cleanliness and integrity of the monolayer. The contact mode image of a typical freshly made SAM shows large underlying (111) terraces and well-defined step edges (Figure 5A), while the lateral force image (Figure 5B), obtained simultaneously as the torsion response of the cantilever, shows the same features but in less detail. At higher magnification (Figure 5C) in the contact mode the hexagonal lattice is observed with a nearest-neighbor distance of 4.9 ± 0.3 Å, corresponding to the standard ($\sqrt{3} \times \sqrt{3}$), R30° lattice structure.[54,55]

In the initial stages of deposition the Ti appears on the surface as clusters that are easily moved by the tip during scanning. This is seen in Figure 6 for $\theta = 1$ where an initial scan of the surface, in either contact (A) or lateral force (B) modes, shows that when the tip comes in contact with a metal cluster, the tip is deflected in both the normal and lateral directions. The clusters

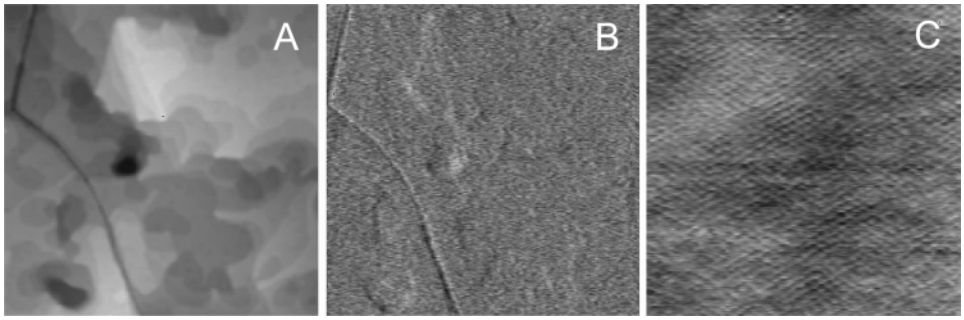

Figure 5. AFM images of a bare CH_3 SAM surface. (A) Contact mode image (1 μm × 1 μm) showing the surface topography. The image reveals the underlying (111) Au terraces and step edges. (B) Simultaneously recorded lateral force image for the scan in panel A. (C) Contact mode imaging in a different, smaller area (17 nm × 17 nm) of the bare SAM reveals the molecular lattice.

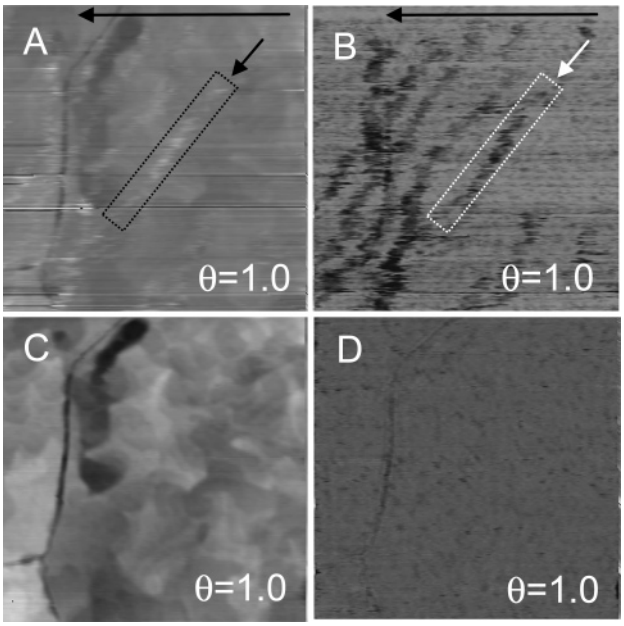

Figure 6. Sequentially taken contact (topography) (A, C) and lateral force (B, D) AFM images (1 μm × 1 μm) of a fixed area of a CH_3 SAM surface after deposition of Ti to coverage $\theta = 1.0$. (A, B) Images show the AFM tip coming into contact with a metal cluster, causing the tip to rise, as seen in the topography, and bend laterally, as seen in the lateral force image. As the tip scans laterally across the surface (in the direction of the top black arrows) a newly contacted cluster is pushed ahead of the tip and typically rolled off to the lower side with the tip passing out of contact to the left. Once the tip is returned to a new position just below the original starting point, the next scan line typically recontacts the cluster and moves it again toward the lower left. The arrows point to a region that shows the typical locus of the motion of a cluster being swept off to the lower left during the first scan (faint white spots in contact mode). After completion of the first scan in the indicated area, most clusters end up being swept off the image area at the lower left. (C, D) With the removal of the clusters, the topographic image regains some sharpness in the resolution of the underlying Au features (C vs A). In the lateral force image (D), note the appearance of small depressions or pits that remain after the clusters are swept off the surface.

are observed to be swept by the tip down the image and slightly to the left. The imaging was done in a series of pairs of scans initiated by a linear scan to the left followed by a reset to the right-hand side and slightly down for the next scan to the left. This causes the tip to initially come into contact with the clusters on the bottom left quadrant of the tip, thus pushing the clusters down and to the left as the pairs of scans continue. The lateral force image shows this effect quite clearly as seen by the circled diagonal track of a cluster as it is continually imaged and pushed down and to the left. Once the initial scan of the surface area is complete, most of the clusters have been swept away, as seen by the absence of these features in either in the topography (C) or lateral force (D) images. The clusters are found to collect at the far edges of the initial scan range and can be observed by increasing the scan area immediately after the sweeping scans are completed. Images of the lattice are possible at this stage, but the detailed features are not as clear as in the bare monolayer. Possible causes include a slight disordering of the monolayer, dulling of the tip caused by reaction with titanium, or clusters adhering to the tip.

While the Ti clusters are easily moved by the AFM tip at low coverages (Figure 6, $\theta = 1.0$), with increasing deposition the clusters start to become firmly attached. For example, Figure 7panels A−C show contact mode images of a surface for $\theta =$ 5 where the images were taken after multiple scans in which all the smaller, more mobile clusters were "swept" aside. It is still possible to see signs of the underlying structure of the Au; however, only the larger Au features are evident and the steps on the surface are not as sharp as in bare monolayer images. The observation of these features indicates that the SAM surface is relatively uniform in the regions bearing small, mobile Ti clusters. The diminishing of the image quality is likely due to contributions from both intrinsic sample degradation and diminishing of the tip sharpness from continued scanning across the rough surface. Note also that some of the clusters at this growth stage are too large to be easily moved by the tip. Even after multiple scans they are not removed from the scan area, as seen by the small, light-colored features, marked by arrows in Figure 7A,B. While the smaller clusters have been moved out of the image, signs of where they originally were are evident in the form of residual, elongated pits, ∼10−50 nm in length. Note the general alignment of the pits in the scan direction, an indication that the elongation is determined by the tip-induced translation across the surface. The depth (∼0.2−1 nm), however, seems intrinsic to the deposition process and is assigned primarily to the chemical attack of the deposited metal atoms on the SAM, in which carbide phases form at the Ti metal/SAM interface. We propose that formation of the pits occurs dynamically by tip-induced fracture at these buried SAM/carbide interfaces to remove the inorganic composite object. The reason some clusters stay in place under tip contact is likely due to the specific details of the carbide−SAM interface topography.

As the deposition increases to the range of tens of Ti atoms per SAM molecule, it becomes difficult to move any of the clusters during scanning. For example, in Figure 7D, for $\theta =$ 10, many smaller clusters remain on the surface after an initial contact mode scan and periodically cause "tip jumps" or streaks in the images when the tip comes in contact with them. With increasing deposition (Figure 7E, $\theta = 20$), more clusters form and the typical sizes increase as the SAM begins to be covered with the metal overlayer. Finally, at the highest coverage shown

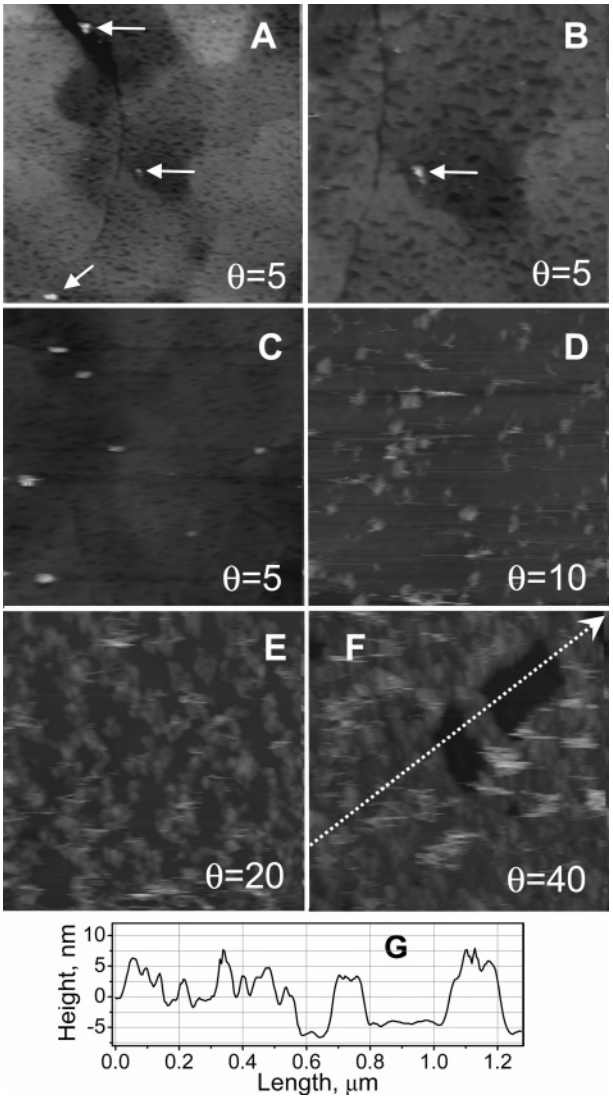

Figure 7. Contact-mode AFM images of SAMs after deposition of Ti. (A) Image (1 μm × 1 μm) of a $\theta = 5$ deposition sample after the surface was swept with the tip for one full scan to remove most of the Ti clusters. Notice the small pits (dark spots) scattered all across the surface, which show where the metal clusters originally grew and reacted with the monolayer. The arrows indicate firmly anchored Ti clusters that were not moved by the tip. (B) Same region as in panel A but a 0.5 μm × 0.5 μm image, which shows the pits in more detail. Typically, the pits are rectangular or oblong as a result of the tip dragging the metal clusters to the left with the initial scan, and they vary in depth from ~0.2−1.0 nm. (C) Image (1 μm × 1 μm) for the $\theta = 5$ sample taken in a different area, which shows both pits and several of the more firmly anchored remaining clusters. (D−F) Images (1 μm × 1 μm) of $\theta = 10$, 20, and 40 samples taken on the first scan after an initial scan to sweep the surface. Note that at these higher coverages the tip is generally unable to move the larger clusters at the forces used, and sweeping has little effect on subsequent scans. The surface density of clusters increases with the amount of deposited metal until at $\theta = 40$ the sample surface is almost entirely covered. The open rectangular patches at $\theta = 40$ appear to be intrinsic to the surface structure, since these types of features with varying shapes and sizes are observed scattered on the surfaces for different samples and surface regions. The presence of these features indicates that complete contact of the surface by the deposited metal requires quite high coverages. The light streaked features arise where the +Z excursion of the cantilever goes beyond the A to D limit. (G) Line scan taken across the dotted line in panel F. Starting from the lower left in panel F, the scan reveals a typical surface topographical modulation of ~4−6 nm for the Ti clusters before the large pits and then shows the depths of the two pits to be ~6−10 nm. This line scan also serves as a calibration for the gray height scales in panels A−F.

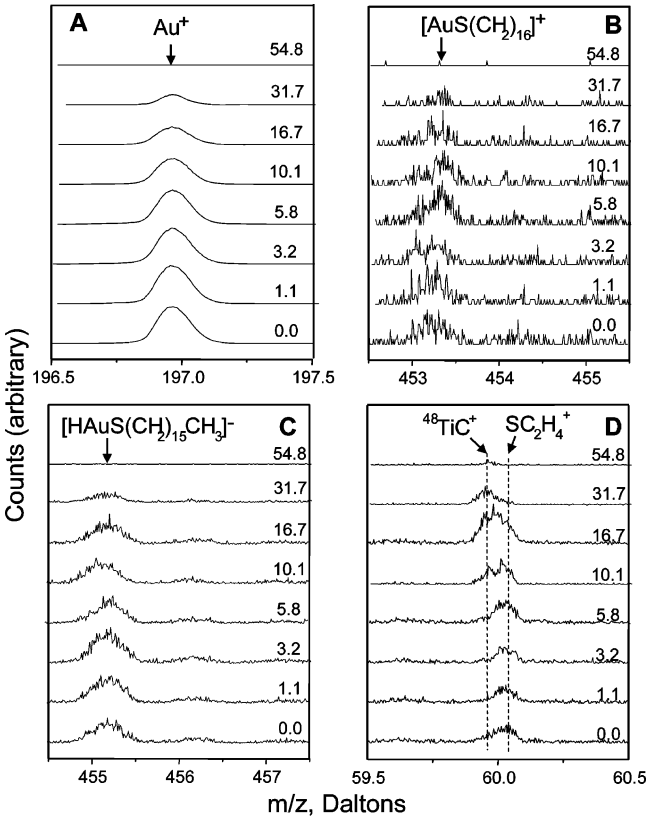

Figure 8. High-resolution ToF−SIMS spectra of selected ion peaks at varying total coverages of deposited Ti on the SAM: (A) Au^+, (B) $AuS(CH_2)_{16}^+$, (C) $HAuS(CH_2)_{16}CH_3^-$, and (D) $^{48}TiC^+$ and $SC_2H_4^+$. The peak intensities are in arbitrary units with different scales for each spectrum, and the Ti coverages are listed on the right of each spectrum.

(Figure 7F, $\theta = 40$), the metal nearly completely covers the SAM. Note the large open areas that are typically observed across different regions of the surfaces. The reason for these areas remains unclear but possibly could be due to a very low sticking probability for the SAM surface in these regions, perhaps due to a high degree of ordering. Some idea of the height scale and surface topography is given in the line scan (Figure 7G) taken across the surface in Figure 7F (line shown by the dotted arrow). Note the typical height modulations of ~4−6 nm for the Ti clusters outside of the pits and the ~6−10 nm depths of the two pits. In general, imaging of the high Ti coverage samples ($\theta > 10$) becomes increasingly difficult as the tip sticks to the surface in many places, likely caused by the silicon tip forming a chemical bond to the Ti surfaces. Force curves done on the surface to find the adhesive force were unsuccessful due to a limited *z* scan range (~100 nm) such that the tip was not able to retract far enough to disengage with the surface.

3.4. Time-of-Flight Secondary Ion Mass Spectrometry: Localized Chemical Degradation. The ToF−SIMS data (Figure 8) were collected primarily to further clarify the nonuniformity and the interface chemistry of the evolving metal overlayers. The nonuniformity is demonstrated by the slow decreases of the Au^+ substrate ion peak (Figure 8A) and the adsorbate molecular peaks ($[AuS(CH_2)_{16}]^+$ in Figure 8B and $[HAuS(CH_2)_{15}CH_3]^-$ in Figure 8C). All of these signals are observed even up to coverages approaching $\theta \sim 30$. Given the shallow sampling depth of the technique (~1 nm), these data are consistent with the gradual covering of the SAM by a Ti overlayer, leaving large fractions of open SAM areas until high deposition amounts, in agreement with the AFM observations.

Evidence for a chemical reaction of Ti with the SAM to form some type of carbide species is supported by the appearance of the $^{48}TiC^+$ peak as the deposition increases (Figure 8D; the accompanying $SC_2H_4^+$ cluster peak is marked for clarity). This feature becomes relatively strong for $\theta \gtrsim 10$ but eventually starts decreasing for $\theta \gtrsim 30$, consistent with the point at which complete Ti overlayers form. Note the lack of a significant $^{48}TiC^+$ signal at the very early deposition times. Since the XPS data clearly indicate early formation of carbide, we conclude that the carbide reactions occur at the metal−SAM contact point directly under a Ti metal cluster where the ion signals would be diminished.

4. Discussion

The combined data for our specific deposition conditions all point to a complex deposition process involving both scattering of the Ti atoms from the SAM surface and severe degradation of the alkyl chains in localized regions across the surface. The main features of the mechanism concluded from our data are summarized pictorially in the schematic in Figure 9. The proposed set of underlying kinetic processes are listed in a generalized way in steps 1−5, with the specific notations for the chemical species defined in the discussion. We note at the outset of this discussion that these results and conclusions are specific to the conditions of a room-temperature sample with a Ti deposition rate of ∼0.15 Ti atom·nm^{-2}·s^{-1} (∼0.033 Ti atom·molecule^{-1}·s^{-1} or equivalently ∼1.0 Ti atom·molecule^{-1} every 30 s).

$$\mathrm{Ti(g)} + \mathrm{SAM} \rightarrow \mathrm{Ti(g)'} + \mathrm{SAM\ (surface\ desorption)} \quad (1)$$

$$\mathrm{Ti(g)} + \mathrm{SAM} \rightarrow \mathrm{Ti(s)\ (surface\ adsorption)} \quad (2a)$$

$$\mathrm{Ti(g)} + \mathrm{SAM} \rightarrow \mathrm{(SAM)^*\ (SAM\ reaction)} \quad (2b)$$

$$n\mathrm{Ti(g)} + \mathrm{(SAM)^*} \rightarrow [(\mathrm{Ti})_n]\mathrm{(SAM)^*\ (Ti\ metal\ cluster\ growth\ at\ reacted\ site)} \quad (2c)$$

$$n\mathrm{Ti(g)} + \mathrm{(SAM)^*} \rightarrow \mathrm{continued\ SAM\ degradation} \quad (2d)$$

$$\mathrm{Ti(s)} \rightarrow \mathrm{Ti(s)\ (surface\ diffusion\ to\ new\ location)} \quad (3a)$$

$$n\mathrm{Ti(s)} \rightarrow [\mathrm{Ti(s)}]_n\ \mathrm{(Ti\ metal\ cluster\ growth\ on\ bare\ SAM)} \quad (3b)$$

$$n\mathrm{Ti(s)} + \mathrm{(SAM)^*} \rightarrow [(\mathrm{Ti})_n]\mathrm{(SAM)^*\ (Ti\ metal\ cluster\ growth\ at\ reacted\ site)} \quad (3c)$$

$$\mathrm{Ti(s)} + \mathrm{SAM} \rightarrow \mathrm{(SAM)^*\ (SAM\ reaction)} \quad (4a)$$

$$\mathrm{Ti(s)} + \mathrm{(SAM)^*} \rightarrow \mathrm{continued\ SAM\ degradation} \quad (4b)$$

$$[(\mathrm{Ti})_n]\mathrm{(SAM)^*} \rightarrow \mathrm{continued\ localized\ SAM\ degradation} \quad (5)$$

It is clear from the QCM and XPS data that a large fraction of the incoming Ti vapor atoms in the initial stages of deposition simply scatter (reflect) off the surface [extreme left of Figure 9 and step 1, where g signifies gas phase]. The scattered species, Ti(g)′, presumably have different momenta and kinetic energies from the incoming atoms and so are labeled with a prime. It is interesting that despite the high chemical reactivity of Ti, as evidenced in later stages by the severe degradation of the molecules, the low initial values of the sticking coefficient (Figure 1) show that a large fraction of the incoming Ti atoms

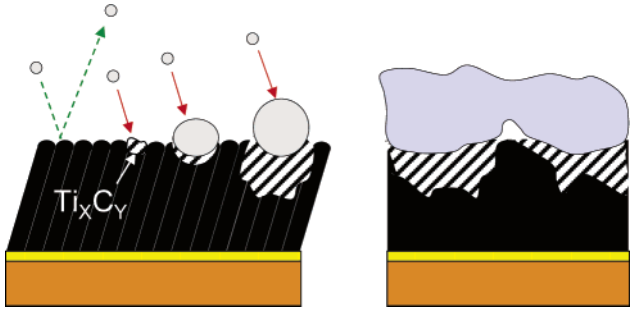

Figure 9. Schematic of the major features arising in the vapor deposition of Ti atoms on a hexadecanethiolate/Au SAM as concluded from the data obtained from multiple in situ characterization probes. The left-hand drawing illustrates for an incoming Ti atom, from left to right, unreactive scattering of an incoming Ti atom off the SAM surface, formation of a carbide reaction product after collision of a Ti atom with the SAM surface, nucleation and growth of a Ti cluster or nanoparticle at a previously reacted surface site, and continued reaction of deposited Ti atoms with -CH_2- units deep into the SAM. The right-hand drawing illustrates the possible characteristics that arise in the later stages of deposition where a complete metal overlayer can form. Note the extensive carbide interphase that forms and the likely formation of voids at the SAM/inorganic interface, which would be caused by the highly nonuniform, chemically heterogeneous character of the growth process across the surface.

are not energetically accommodated at the bare SAM and readily desorb. As the deposition continues from the initial stages, an increasing number of Ti atoms are accommodated at the surface, either as new nucleation sites or adsorbed at existing nucleation sites. This could occur by a combination of thermal accommodation (step 2a, where s signifies surface) to simply lower the kinetic energy of the Ti, thereby preventing desorption from the surface, and immediate chemical reaction [step 2b, where (SAM)* is some generalized type of initial reaction product], most likely initially with a CH_3 group. Reaction could occur if the impacting Ti atom is on the high end of the Boltzmann energy tail, sufficient to overcome an activation barrier, and/or if the adsorption site is a surface defect of some type that facilitates the energetic or configurational requirements of the reaction. Such defects could include, for example, a disordered terminal chain segment or a molecular ensemble that has been topographically elevated due to underlying substrate defects. Once reacted, these sites could act as nucleation points for further incoming Ti(g) atoms to form Ti metal clusters (step 2c) or could continue to degrade (step 2d). Steps 3a−c show adsorbed Ti(s) atoms diffusing across the surface (step 3a) and collecting to form metal clusters on the bare SAM (step 3b) and at initially reacted SAM sites (step 3c). The growth of clusters with unreacted Ti atoms contacting the SAM surface, however, seems somewhat unlikely since the combination of the XPS, IRS, and AFM data suggests that reaction to carbide starts in the very initial stages of deposition so the probability of unreacted metal atoms directly in contact with the SAM is small. In steps 4a,b, adsorbed Ti(s) atoms diffuse and react at sites on the bare SAM or at previously reacted sites, respectively.

The continual increase in the sticking coefficient with increasing Ti coverage implies that an increasing number of nucleation centers appear, which can either accommodate incoming Ti(g) atoms or trap surface-diffusing Ti(s) atoms. Overall, our data suggest the nucleation centers mostly consist of reacted top tail sections of the chains, particularly the CH_3 units (IRS), and continue to react with increasing Ti coverage [step 2c for Ti(g) and step 4b for Ti(s)] to form carbide products (XPS) with increasingly deep monolayer damage (AFM). As the Ti surface coverage grows, it is important to note that

the AFM images (Figure 7) show a significant fraction of open surface, even up to tens of Ti atoms adsorbed per SAM molecule. This result is supported by the ToF−SIMS data (Figure 8), which indicate that long deposition times are required to completely block the SAM and prevent ejection of SAM and Au substrate fragments in the SIMS experiment. These data suggest that there may be bare areas of the SAM surface for which the sticking coefficient remains at the low values observed in the initial stages of the deposition. This could arise, for example, if the initial nucleation required a reactive surface defect of some type such that any local region free of such defects would remain bare until late in the deposition.

As the deposition proceeds to values of $\theta \gtrsim 5$, the IRS and AFM data indicate attack begins to proceed deep into the SAM, progressing along the methylene units of the alkyl chains. The AFM data clearly show that this degradation proceeds at growing Ti cluster sites, which suggests a mechanism involving diffusion of Ti atoms from the growing cluster into the contiguous SAM molecules and down the chains, either on the originally reacted chain or onto a neighboring unreacted chain. This seems reasonable in view of the extensive destruction of the hydrocarbon material, which should lead to a nanoporous carbide/hydride material with multiple diffusion channels for Ti atoms.

In the final stages of the deposition, a complete overlayer forms. As depicted in Figure 9, however, it is likely that the highly nonuniform morphology of the Ti film, especially with open areas such as those seen in the AFM images (Figure 7F,G), will likely lead to incomplete contact across the surface, that is, the formation of voids at the SAM/Ti interface.

5. Conclusions

The combination of four in situ surface analysis techniques shows that under the conditions of Ti deposition at ∼0.15 Ti atom·nm^{-2}·s^{-1} onto the surface of an ambient temperature CH_3-$(CH_2)_{15}$S/Au{111} SAM, a very nonuniform Ti overlayer forms in a process in which a large fraction of impinging Ti atoms do not stick to the bare SAM surface despite the high reactivity of Ti atoms with the SAM molecules. Initial nucleation of Ti at the surface appears to involve primarily chemical interaction with the CH_3 groups of the SAM to form carbide, and presumably hydride, products. Growth of Ti clusters appears to be concentrated at these scattered reaction centers. The SAM molecules in the local vicinity are subsequently degraded to inorganic products, progressing deeper into the SAM as the deposition proceeds with reaction reaching depths of ∼0.5 nm, approximately halfway along the alkyl chains, to give a highly heterogeneous inorganic/organic nanocomposite. A complete overlayer does not form until metal coverages approach 50 Ti atoms per SAM molecule. The nonuniform morphology of the growing film until these last stages suggests that the underlying SAM/Ti interface is not complete and exhibits voids.

These data show that for applications such as molecular electronics devices, where the formation of a clean, uniform metal/SAM interface is typically desired, the use of Ti may be highly problematic, suffering from both discontinuities across the contact area and the presence of inorganic products such as nonstoichiometric carbides and hydrides. On the other hand, by the use of careful control of the deposition conditions, kinetic energy of the metal atoms in the vapor, sample temperature, background gas pressure, and SAM chemical composition, there would appear to be opportunities to synthesize unique types of thin film inorganic composites with unique and useful properties for a variety of applications. The most promising variables would appear to be the control of the incoming atom energies and momenta and the sample temperatures. Experiments in these directions are now underway in our laboratories.

Acknowledgment. We gratefully acknowledge financial support from the National Science Foundation (NSF), the Defense Advanced Project Agency, The Air Force Office of Scientific Research, and the Penn State NSF MRSEC program.

Supporting Information Available: Preparation and characterization of $CD_3(CD_2)_7(CH_2)_8SH$ and XPS Au 4f and S 2p spectra. This material is available free of charge via the Internet at http://pubs.acs.org.

References and Notes

(1) Jung, D. R.; Czanderna, A. W. *Crit. Rev. Solid State* **1994**, *19*, 1−54.
(2) Herdt, G. C.; King, D. E.; Czanderna, A. W. *Z. Phys. Chem.* **1997**, *202*, 163−196.
(3) Hooper, A.; Fisher, G. L.; Konstadinidis, K.; Jung, D.; Nguyen, H.; Opila, R.; Collins, R. W.; Winograd, N.; Allara, D. L. *J. Am. Chem. Soc.* **1999**, *121*, 8052−8064.
(4) Fisher, G. L.; Hooper, A. E.; Opila, R. L.; Allara, D. L.; Winograd, N. *J. Phys. Chem. B* **2000**, *104*, 3267−3273.
(5) Fisher, G. L.; Walker, A. V.; Hooper, A. E.; Tighe, T. B.; Bahnck, K. B.; Skriba, H. T.; Reinard, M. D.; Haynie, B. C.; Opila, R. L.; Winograd, N.; Allara, D. L. *J. Am. Chem. Soc.* **2002**, *124*, 5528−5541.
(6) Walker, A. V.; Tighe, T. B.; Reinard, M. D.; Haynie, B. C.; Allara, D. L.; Winograd, N. *Chem. Phys. Lett.* **2003**, *369*, 615−620.
(7) Walker, A. V.; Tighe, T. B.; Stapleton, J.; Haynie, B. C.; Upilli, S.; Allara, D. L.; Winograd, N. *Appl. Phys. Lett.* **2004**, *84*, 4008−4010.
(8) Walker, A. V.; Tighe, T. B.; Cabarcos, O. M.; Reinard, M. D.; Haynie, B. C.; Uppili, S.; Winograd, N.; Allara, D. L. *J. Am. Chem. Soc.* **2004**, *126*, 3954−3963.
(9) Zhou, C.; Deshpande, M. R.; Reed, M. A.; Jones, L.; Tour, J. M. *Appl. Phys. Lett.* **1997**, *71*, 611−613.
(10) Collet, J.; Vuillame, D. *Appl. Phys. Lett.* **1998**, *73*, 2681−2693.
(11) Allara, D. L.; Dunbar, T. D.; Weiss, P. S.; Bumm, L. A.; Cygan, M. T.; Tour, J. M.; Reinerth, W. A.; Yao, Y.; Kozaki, M.; Jones, L. *Ann. N.Y. Acad. Sci.* **1998**, *852*, 349−370.
(12) Collier, C. P.; Wong, E. W.; Belohradsky, M.; Raymo, F. M.; Stoddart, J. F.; Kuekes, P. J.; Williams, R. S.; Heath, J. R. *Science* **1999**, *285*, 391−394.
(13) Chen, J.; Reed, M. A.; Rawlett, A. M.; Tour, J. M. *Science* **1999**, *286*, 1550−1552.
(14) Chen, J.; Wang, W.; Reed, M. A.; Rawlett, A. M.; Price, D. W.; Tour, J. M. *Appl. Phys. Lett.* **2000**, *77*, 1224−1226.
(15) Reed, M. A.; Chen, J.; Rawlett, A. M.; Price, D. W.; Tour, J. M. *Appl. Phys. Lett.* **2001**, *78*, 3735−3737.
(16) Collier, C. P.; Mattersteig, G.; Wong, E. W.; Luo, Y.; Beverly, K.; Sampaio, J.; Raymo, F. M.; Stoddart, J. F.; Heath, J. R. *Science* **2000**, *289*, 1172−1175.
(17) Collier, C. P.; Jeppesen, J. O.; Luo, Y.; Perkins, J.; Wong, E. W.; Heath, J. R.; Stoddart, J. F. *J. Am. Chem. Soc.* **2001**, *123*, 12632−12641.
(18) Metzger, R. M.; Xu, T.; Peterson, I. R. *J. Phys. Chem. B* **2001**, *105*, 7280−7290.
(19) Chen, J.; Reed, M. A. *Chem. Phys.* **2002**, *281*, 127−145.
(20) Chang, S. C.; Li, Z. Y.; Lau, C. N.; Larade, B.; Williams, R. S. *Appl. Phys. Lett.* **2003**, *83*, 3198−3200.
(21) Vuillaume, D.; Lenfant, S. *Microelectron. Eng.* **2003**, *70*, 539−550.
(22) Lenfant, S.; Krzeminski, C.; Delerue, C.; Allan, G.; Vuillaume, D. *Nano Lett.* **2003**, *3*, 741−746.
(23) (a) McCreery, R.; Dieringer, J.; Solak, A. O.; Snyder, B.; Nowak, A. M.; McGovern, W. R.; DuVall, S. *J. Am. Chem. Soc.* **2003**, *125*, 10748−10758. (b) McCreery, R.; Dieringer, J.; Solak, A. O.; Snyder, B.; Nowak, A. M.; McGovern, W. R.; DuVall, S. *J. Am. Chem. Soc.* **2004**, *126*, 6200.
(24) de Boer, B.; Frank, M. M.; Chabal, Y. J.; Jiang, W. R.; Garfunkel, E.; Bao, Z. *Langmuir* **2004**, *20*, 1539−1542.
(25) Jung, G. Y.; Ganapathiappan, S.; Li, X.; Ohlberg, D. A. A.; Olynick, D. L.; Chen, Y.; Tong, W. M.; Williams, R. S. *Appl. Phys. A* **2004**, *78*, 1169−1173.
(26) McCreery, R. L. *Chem. Mater.* **2004**, *16*, 4477−4496.
(27) Stewart, D. R.; Ohlberg, D. A. A.; Beck, P. A.; Chen, Y.; Williams, R. S.; Jeppesen, J. O.; Nielsen, K. A.; Stoddart, J. F. *Nano Lett.* **2004**, *4*, 133−136.
(28) Lau, C. N.; Stewart, D. R.; Williams, R. S.; Bockrath, M. *Nano Lett.* **2004**, *4*, 569−572.

(29) Haick, H.; Ambrico, M.; Ghabboun, J.; Ligonzo, T.; Cahen, D. *Phys. Chem. Chem. Phys.* **2004**, *6*, 4538−4541.
(30) Konstadinidis, K.; Taylor, A. J.; Miller, A. C.; Opila, R. L. *J. Adhes.* **1994**, *46*, 197−213.
(31) Tachibana, T.; Williams, B. E.; Glass, J. T. *Phys. Rev. B* **1992**, *45*, 11975−11981.
(32) Bodo, P.; Sundgren, J. E. *J. Vac. Sci. Technol. A* **1984**, *2*, 1498−1502.
(33) Bodo, P.; Sundgren, J. E. *J. Appl. Phys.* **1986**, *60*, 1161−1168.
(34) Ohuchi, F. S.; Freilich, S. C. *J. Vac. Sci. Technol. A* **1986**, *4*, 1039−1045.
(35) Du, M.; Opila, R. L.; Case, C. *J. Vac. Sci. Technol. A* **1998**, *16*, 155−162.
(36) Konstadinidis, K.; Zhang, P.; Opila, R. L.; Allara, D. L. *Surf. Sci.* **1995**, *338*, 300−312.
(37) (a) Thran, A: Zaporojtchenko, V.; Faupel, F. *Phys. Rev. Lett.* **1999**, *82*, 1903−1906. (b) Zaporojtchenko, V.; Behnke, K.; Strunskus, T.; Faupel, F. *Surf. Sci.* **2000**, *454*, 412−416.
(38) Allara, D. L.; Nuzzo, R. G. *Langmuir* **1985**, *1*, 52−66.
(39) Nuzzo, R. G.; Dubois, L. H.; Allara, D. L. *J. Am. Chem. Soc.* **1990**, *112*, 558−569.
(40) Laibinis, P. E.; Whitesides, G. M.; Allara, D. L.; Tao, Y. T.; Parikh, A. N.; Nuzzo, R. G. *J. Am. Chem. Soc.* **1991**, *113*, 7152−7167.
(41) MacPhail, R. A.; Strauss, H. L.; Snyder, R. G.; Elliger, C. A. *J. Phys. Chem.* **1984**, *88*, 334−341.
(42) Laibinis, P. E.; Nuzzo, R. G.; Whitesides, G. M. *J. Phys. Chem.* **1992**, *96*, 5097−5105.
(43) Braun, R. M.; Blenkinsopp, P.; Mullock, S. J.; Corlett, C.; Willey, K. F.; Vickerman, J. C.; Winograd, N. *Rapid Commun. Mass. Spectrom.* **1998**, *12*, 1246−1252.
(44) Other imaging modes were considered but were ultimately not possible to apply in our experiments. For example, in the case of tapping mode, where the cantilever is oscillated in the *Z* direction, vacuum conditions cause the cantilever resonance frequency to become too sharp to accommodate the surface-tip force-induced frequency shifts that allow imaging [for example, see, Garcia, R.; Perez, R. Dynamic Atomic Force Microscopy Measurements. *Surf. Sci. Rep.* **2002**, *47*, 197−301]. The much less common, noncontact methods might be useful but this capability was not in operation in our system at the time of the experiments. Preliminary trials are now being planned to evaluate this mode for our application.
(45) To achieve high signal/noise, custom-built phase-locked loop setups were utilized with a Hewlett-Packard 8656B signal generator, an EG&G 5202 lock-in amplifier, two Hewlett-Packard 3478A multimeters, and a Hewlett-Packard 53181A frequency counter. The latter two were interfaced to a PC by use of National Instruments LabVIEW software. This setup gave a ± 0.05 Hz noise level, which is equivalent to $\theta_M = \pm 0.02$. The SAM-functionalized QCM crystal and Au reference crystals were placed side by side, the same distance from the deposition source and the sample QCM holder temperature controlled at ∼25 °C (the approximate SAM sample temperatures in the actual analysis experiments) by use of circulated water. The SAM QCM crystals (Cold Springs R&D, Syracuse, NY) were highly polished on one side to an rms roughness (tapping mode AFM) of 0.1−0.2 nm, which resulted in the QCM SAM surfaces having near identical rms roughnesses to those of the SAMs prepared on silicon substrates. Both QCMs had movable shutters to independently control access of the metal flux to the surfaces. Just prior to a set of measurements, the sample was blocked while the reference shutter was opened to allow the Ti flux to strike the reference QCM surface and condense many layers of Ti to provide a fresh Ti surface with unit efficiency in condensing Ti atoms. Subsequently both shutters were opened to make continuous measurements of the total flux delivered (reference QCM) and the amount condensed on the SAM.
(46) Sticking probabilities were estimated from the area ratios of the metal core level peaks to the Au 4f and C 1s peaks by use of instrument-determined cross sections [e.g., see Briggs, D.; Grant, J. T., Eds. *Surface Analysis by Auger and X-ray Photoelectron Spectroscopy*; IM Publications: West Sussex, U.K., 2003]. Estimates were not made above $\theta = 10$ because of the increasing uncertainty in applying the necessary photoelectron mean free path corrections to the heterogeneous Ti films with varying thicknesses of metal across the surface (e.g., as shown by our AFM data).
(47) Georgiev, D. G.; Baird, R. J.; Newaz, G.; Auner, G.; Witte, R.; Herfurth, H. *Appl. Surf. Sci.* **2004**, *236*, 71−76.
(48) Wagner, C. D.; Naumkin, A. V.; Kraut-Vass, A.; Allison, J. W.; Powell, C. J., Rumble, J. R.. Eds. *NIST X-ray Photoelectron Spectroscopy Database 20*, version 3.4 (Web version); National Institute of Standards and Technology: Gaithersburg, MD, 2003.
(49) Schmiedgen, M.; Graat, P. C. J.; Baretzky, B.; Mittemeijer, E. J. *Thin Solid Films* **2002**, *415*, 114−122.
(50) In general, because of the heterogeneous nature of the deposited Ti (e.g., see AFM data), quantitative analysis of the various core level peaks in the XPS spectra was not performed.
(51) Parikh, A. N.; Allara, D. L. *J. Chem. Phys.* **1992**, *96*, 927−945.
(52) Strunksus, T.; Grunze, M.; Kochendoerfer, G.; Wöll, Ch. *Langmuir* **1996**, *12*, 2712−2725.
(53) It is interesting to note that if there were a kinetic isotope effect for Ti reaction with a C−H(D) bond, one would expect that the C−D bonds would be attacked more slowly (by factors reaching as high as nearly half an order of magnitude), all other factors being equal. For such an isotope effect, one would expect in the case of a fully protiated molecule that the top part of the SAM would react even more rapidly (selectively) compared to the bottom part than indicated in Figure 3 for the molecule with the deuterated top.
(54) Poirier, G. E.; Tarlov, M. J. *Langmuir* **1994**, *10*, 2853−2856.
(55) Delamarche, E.; Michel, B.; Gerber, C.; Anselmetti, D.; Guntherodt, H. J.; Wolf, H.; Ringsdorf, H. *Langmuir* **1994**, *10*, 2869−2871.